Facile deposition of NiFe-LDH ultrathin film on pyrolytic graphite sheet for oxygen evolution reaction in alkaline electrolyte

Cipriano B. Gozzo [a,*], *Mario R.S. Soares* [b,d], *Fabrício B. Destro* [c], *João B.S. Junior* [d], *Edson R. Leite* [b,d]

[a] *University of São Paulo (USP), São Carlos Institute of Chemistry (IQSC), São Carlos, SP, Brazil*
[b] *Federal University of São Carlos (UFSCar), Department of Chemistry, São Carlos, SP, Brazil*
[c] *Federal University of São Carlos (UFScar), Department of Materials Engineering, São Carlos, SP, Brazil*
[d] *Brazilian Nanotechnology National Laboratory (LNNano), Brazilian Center for Research in Energy and Materials (CNPEM), Campinas, SP, Brazil*

HIGHLIGHTS

- Facile deposition of NiFe25 on surface of PGS.
- NiFe25/PGS showed a nanosheet morphology.
- NiFe25/PGS was effective for oxygen evolution reaction (332 mV at 10 mA cm^{-2}).
- PGS proved to be a better substrate for the alkaline OER in comparison of GC and FTO.

GRAPHICAL ABSTRACT
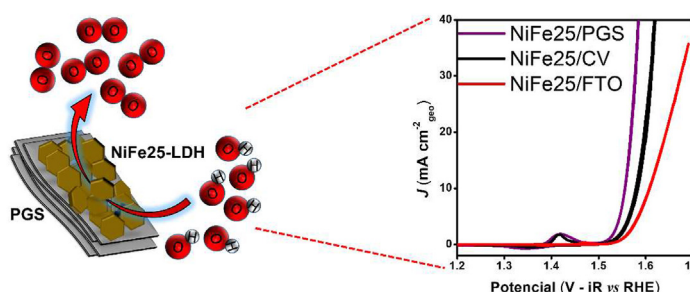
ARTICLE INFO

ABSTRACT

NiFe-layered doubly hydroxide (LDH) is one of the most active materials for hydroxyl oxidation in an alkaline electrolyte. In this study, we explored a facile method of depositing NiFe-LDH catalyst on pyrolytic graphite sheets (PGSs) to explore the synergistic effects at the substrate—electrocatalyst interface. The catalyst was electrodeposited on PGSs using chronoamperometry. The homogeneous distribution of the catalyst with nanosheet morphology on the PGS's surface produced an ultrathin film. The NiFe25/PGS sample showed a low overpotential (332 mV) and Tafel slope (33 mV dec^{-1}). The fitting of the Nyquist plots was performed using an equivalent circuit, and the NiFe25/PGS (1.69 Ω) sample showed the lowest charge transfer resistance among the studied catalysts. In addition, PGS proved a better substrate for the alkaline oxygen evolution reaction compared to glassy carbon and fluorine-doped tin oxide.

Introduction

Recently, studies have been primarily focused on sustainable energy technologies in electrochemical energy conversion and storage [1]. Sustainable energy technologies form a fundamental research area because they can supply the growing demand for energy and mitigate the environmental impact caused by fossil fuels [2]. Hydrogen fuels are an important alternative to conventional fuels because they can be obtained from renewable sources with clean energy [3]. Among several works in this field, the production of hydrogen (hydrogen evolution reaction (HER)) and oxygen (oxygen evolution reaction (OER)) from the photo- and electrochemical reactions in alkaline electrolytes has been widely studied [4—8]. In this process, HER ($4H_2O_{(l)} + 4e^- \rightarrow 4H_{2(g)} + 4OH^-_{(aq)}$) and OER ($4OH^-_{(aq)} \rightarrow 2O_{2(g)} + 2H_2O_{(l)} + 4e^-$) occur on the surface of the cathode and anode, respectively [9].

OER involves a complex process involving four electrons, and this is the bottleneck in hydrogen production with a high potential due to slow kinetics. Ruthenium oxide ($RuO2$) and iridium oxide ($IrO2$) are considered the state-of-the-art electrodes for hydroxyl oxidation [10,11]. However, these catalysts have some undesirable drawbacks, such as high cost and poor stability [2,12,13], for broad-scale applications. Therefore, alternative electrodes based on transition metals with low production cost, high catalytic activity, and stability in alkaline electrolyte must be explored.

Recently, different catalytic structures based on transition metals, such as perovskite [7], spinel [12], phosphide [14], carbide [15], and layered double hydroxide (LDH) [16], showing good performance in OER have been explored. Among these, LDH is the most attractive material to replace catalysts based on precious metals owing to its high catalytic activity in alkaline environments [17,18].

Subbaraman et al. [19] has reported a decreasing electrocatalytic trend among LDHs in hydroxyl oxidation: Ni > Co > Fe > Mn. However, it is well known that the introduction of Fe to Ni oxyhydroxides improves the catalytic activity for OER [20,21]. NiFe-LDH is the most active material for hydroxyl oxidation among the LDH structures exhibiting the best performances at approximately 30% Fe [2,22,23]. Diogini et al. [17] reported that the catalytic activity increased due to the synergy between the Fe and Ni sites through O-bridged Fe—Ni reaction centers. NiFe-LDH is a widely studied subject in the literature, as demonstrated by many researches on the application of this material in OER [24—32].

Another challenge is related to the synthesis of NiFe-LDHs because the bulk material shows poor conductivity, whereas the nanostructures and thin films show a 100-fold greater ionic conductivity [33,34]. Different structures including the hierarchical architecture of LDH [34], 3D structures using nickel foam [35], ultrathin films [36,37] and core-shell nanoparticles [38] have been studied to enhance the production of O_2.

In addition to the synthesis process, the support electrode must be analyzed. Although there is no standard substrate for OER, the interaction between the catalyst and the support substrate is fundamental, and this can improve the electrocatalytic activity in hydroxyl or water oxidation reactions [39].

Wei et al. [40] reported how the different substrates influence the catalytic activity of NiFe-LDH in OER. They electrodeposited the catalysts on gold (Au), copper (Cu), titanium (Ti), and tin-doped indium oxide (ITO) substrates and tested for hydroxyl oxidation using 1-mol L−1 KOH electrolyte. This study showed an improvement in the catalytic kinetics, with an increase in the catalytic activity in the following order: NiFe/Ti < NiFe/ITO < NiFe/C < NiFe/Cu < NiFe/Au. An extensive range of different support electrodes used in oxygen catalysis has been previously reported [39,41,42].

Based on the importance of substrates in electrocatalysis, pyrolytic graphite sheets (PGSs) are presented as an interesting material due of several advantageous characteristics: good thermal conductivity (700—1950 W m−1 K−1), simple handling (flexible, can be folded, and cut easily), variable thicknesses (10—100 μm), and excellent electrical conductivity (1000 S cm−1 for a thickness of 70 μm) [43]. This substrate has a honeycomb-like structure with the graphite sheets arranged in a particular orientation. Several studies have reported PGS as adsorption substrates to detect superfluidity in helium monolayers [44], aluminum ion battery electrodes [45], and thermal conductors in proton exchange membrane fuel cells [46].

This study proposes the enhancement of the catalytic activity of NiFe—LDH in OER using PGS as a substrate. Our research group previously reported that LaNi0.4Fe0.6O3 structures deposited on PGS show a lower overpotential (η) and charge transfer resistance (R_{ct}) compared with those of the same material deposited on glassy carbon (GC). Furthermore, LaNi0.4Fe0.6O3/PGS showed a low Tafel slope and good stability in an alkaline electrolyte [47]. In the present study, the main objective is to perform a facile electrodeposition of NiFe-LDH ultrathin film on the surface of PGS and investigate its properties in the hydroxyl oxidation. Finally, the effectiveness of the PGS support electrode is also evaluated against other common substrates.

Experimental procedure

Materials

$Ni(NO_3)_2 \cdot 6H_2O$ (≥98.5%) and $Fe(NO_3)_3 \cdot 9H_2O$ (≥98.5%) were purchased from Sigma Aldrich. PGS (model EYG with 70-m thickness) was purchased from Panasonic®.

Electrocatalyst preparation

The thin-film NiFe-LDH with 25% iron on PGS (NiFe25/PGS) was prepared by electrodeposition using chronoamperometry. First, $Ni(NO_3)_2 \cdot 6H_2O$ and $Fe(NO_3)_3 \cdot 9H_2O$ were dissolved in Millipore deionized (DI) water and then, a potential of −1 V was applied for 200 s. A three-electrode electrochemical cell (Fig. S1) was used for the deposition of the electrocatalyst with PGS as the working electrode (0.5 cm^2) and platinum (Pt) and Ag/AgCl@3 mol L^{-1} as the counter and reference electrodes, respectively. Electrodeposition of LDH structures with other percentages of Fe (10% and 50%), as well as pure phases (Ni only and Fe only), was performed as a comparison parameter for the evaluation of the catalytic

activity. The solutions prepared for electrodeposition are listed in Table S1.

Structural characterization

X-ray diffraction (XRD) was performed using a Shimadzu diffractometer model 6000 operating with CuK$_\alpha$ radiation ($\lambda = 0.154$ nm) and data collection in 2θ ranging from 10° to 80° with a scan rate and increment of 0.2°/min and 0.02°, respectively. A Grazing Incidence X-ray Diffraction (GIXRD) was performed in a D8 advanced Bruker diffractometer with 2θ ranging from 10° to 80°. Raman spectroscopy was performed using a 638-nm laser using the Horiba Scientific model T64000 Raman spectrometer with an area of 50 × 50 μm. The surface oxidation states and chemical composition were investigated by X-ray Photoelectron Spectroscopy (XPS) in an ESCA spectrometer (ScientaOmicron, Germany) with a high-performance hemispheric analyzer (EA 125). Monochromatic AlK$_\alpha$ radiation (1486.6 eV) was used as the excitation source with the energy steps of 0.5 and 0.05 eV for survey and high-resolution spectra, respectively. The C 1s peak was used as a reference binding energy calibration, and the XPS spectra was examined with CasaXPS software, wherein the core-level signals were fitted with Gaussian-Lorentzian functions and background subtraction according to Shirley method.

Morphological characterization

The morphological features were examined with an Inspect F50 scanning electron microscope equipped with a Schottky field emission source (FESEM) and a scanning transmission electron microscope (STEM) Titan Themis Cubed (both from FEI Company). STEM analysis was performed in a carbon grid containing the electrodeposited NiFe-LDH catalyst (Fig. S2). First, a metallic contact was made with the grid carbon and then, dipped in a solution containing Ni^{2+} and Fe^{3+} in Millipore DI water, followed by the application of a potential of −1 V for 50 s. Roughness, thickness, and surface morphology were analyzed using a Bruker-MultiMode8 atomic force microscope (AFM). The FESEM and AFM studies were performed in NiFe-LDH catalyst deposited on PGS.

Electrochemical characterization

All electrochemical properties were evaluated using a Teflon three-electrode electrochemical cell with Pt as the counter electrode and Ag/AgCl@3 mol L^{-1} as the reference electrode. 1-mol L^{-1} NaOH was used as the electrolyte. The potentials were converted into reference hydrogen electrode (RHE) via Equation (1):

$$E_{RHE} = E_{REF} + (0.059 \times \text{pH}) + E_{MEA} \tag{1}$$

where E_{MEA} and E_{REF} are the measured and reference potentials, respectively.

The OER activities were monitored using cyclic voltammetry (CV), recorded in a potential range of 1.10−1.80 V vs. RHE with a scan rate of 5 mV s−1. CV curves were normalized by subtracting the electrolyte resistance to avoid the effects of Ohmic drop. η values were acquired at 10 mA cm−2 using Equation (2):

$$\eta = ERHE - 1.23V \ vs. \ RHE \tag{2}$$

Electrochemical impedance spectroscopy (EIS) was conducted at 1.5 V vs. RHE in the frequency range between 10−2−105 Hz. The Nyquist plots were analyzed using ZView 3.1 software. EIS spectra were modeled after the Armstrong and Henderson equivalent electric circuit (Fig. S4). Details about the EIS analysis can be found in the supplementary information. The stability of the catalyst was evaluated using chronoamperometry measurements over 10 h with an applied potential of 1.56 V vs. RHE.

Results and discussion

To determine the structural properties of the commercial PGS, XRD and Raman analysis were performed. The XRD pattern of PGS shows a characteristic preferential orientation (Fig. S4). The peaks around 26.5° and 54.7° refer to the oriented graphite carbon planes (002) and (004), respectively, and this structure has a layer spacing of ~3.36 Å. This pattern is in agreement with the crystallographic record found in the inorganic crystal structure database (ICSD-76767) [48]. To examine the growth of the NiFe25-LDH catalyst deposited on PGS, GIXRD analysis was performed. Fig. 1 shows the GIXRD pattern of NiFe25/PGS; however, only the peaks of the oriented graphite carbon planes were observed. The peak at approximately 17° was attributed to graphite oxide [49]. This result suggests that NiFe-LDH grew with an amorphous structure on the PGS surface. A second hypothesis could be that an ultrathin film grew, which did not allow the observation of diffraction planes.

The Raman spectra of commercial PGS without the catalyst can be observed in Fig. 2a. Characteristic graphite bands were
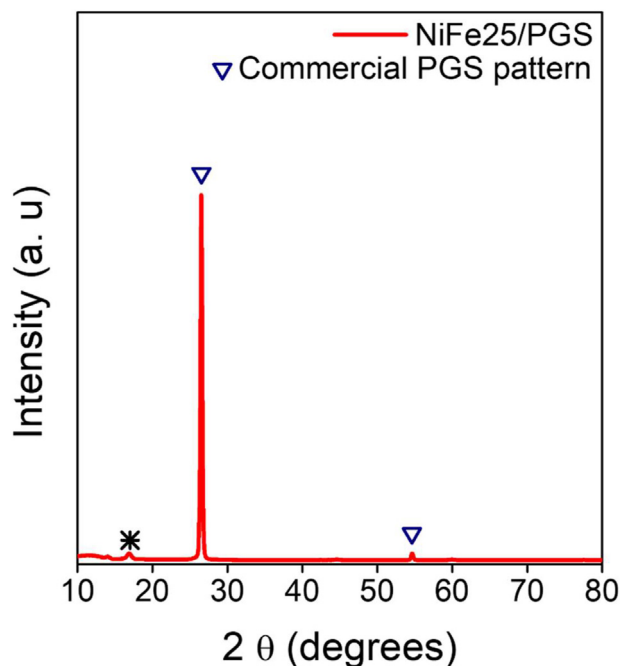

Fig. 1 − Grazing incidence diffraction X-ray (GIXRD) pattern of NiFe25/PGS electrocatalyst.

found: the vibration in the plane of the ring structure with A1g symmetry is characterized by the D band at 1327 cm−1, and the 2D band at 2657 cm−1 denoted the harmonic vibration of the D band. The stretching vibration in the sp2 carbon plane with E2g symmetry is represented by the G band at 1577 cm^{-1} [50].

Because it was not possible to observe the XRD patterns of the NiFe25/PGS catalyst, Raman spectroscopy was performed to determine the vibrational modes of this material. Fig. 2b show the Raman spectra in the lower region of PGS and NiFe25/PGS. The bands assigned to NiFe-LDH were not found in the XRD results. This material has characteristic vibrational modes in which the bands at approximately 450, 520, and 700 cm−1 can be characterized as Ni−O stretching vibration, defective, and the Fe−O disordered vibrations, respectively [51]. This corroborates the previous results, again suggesting an amorphous structure on PGS or the growth of an ultrathin film.

XPS was performed to confirm the presence of the NiFe-LDH electrocatalyst on the surface of PGS. The elemental composition and the chemical states found on the surface are observed in Fig. 3a−d. It was found that the survey spectrum of NiFe25/PGS clearly exhibits the element signals corresponding to Ni, Fe, O, and C (Fig. 3a).

Fig. 3b shows a high-resolution XPS spectrum of Ni 2p. A doublet splitting into Ni 2p1/2 and Ni 2p3/2 caused by a spin-orbit interaction was noted. The spectrum was well fitted and deconvoluted into four peaks. The binding energies at 856.3 and 873.9 eV of the doublet, and 861.9 and 879.9 eV of the satellite peaks are all characteristic of Ni^{2+} sites [52]. The Fe 2p was well fitted with two peaks corresponding to Fe 2p1/2 and Fe 2p3/2 (Fig. 3c). The energies found at the Fe 2p level (724.7 and 712.9 eV) belong to the Fe^{3+} oxidation state [53]. Two peaks were observed at the O 1s region (Fig. 3d). The energies of 532.5 and 531.6 eV were assigned to chemisorbed molecular water and hydroxyl groups attached to the metals (M − OH) on the surface [54,55].

An analysis of the material growth was evaluated using FESEM. First, an analysis using backscattered electrons was performed in the region of PGS with and without the NiFe-LDH electrocatalyst (Fig. 4a). The blue line represents the PGS surface on which the catalyst was deposited, and the brighter region is attributed to nickel and iron with atomic numbers greater than carbon [56].

Another feature that corroborating the NiFe deposition on PGS is the morphology of the electrocatalyst. Thus, an analysis using a secondary electron (SE) detector was performed to observe the morphologies of PGS and electrodeposited material. The commercial PGS surface consisted of several stacked graphite sheets (Fig. S5), whereas NiFe-LDH had nanosheet morphology [57,58].

Fig. 4b showed the SE results in the electrocatalyst region. The characteristic nanosheet morphology of this material was observed, proving homogeneous electrodeposition on the PGS surface. A comparison was made among the NiFe-LDH, Ni-LDH, and Fe-LDH structures. While Ni-LDH and NiFe-LDH structures showed nanosheet morphology, Fe-LDH catalyst had cauliflower morphology [59] (Figs. S6a−d). Interestingly, the introduction of iron in Ni-LDH contributed to a homogeneous distribution without cracks, as observed in the compound containing Ni only. Once the electrodepositions were subjected to the same potential, iron provided the driving force to the formation of the nanosheet morphology without surface cracks.

To understand the NiFe-LDH growth on the PGS surface, an AFM analysis was performed, whose results can be observed in Fig. 5a−d. It was found that the catalyst was already anchored within 10 s of deposition (Fig. 5b), and an increase in the electrodeposition time led to a small increase in the root mean square roughness (Fig. 5c and d). These observations indicate that the negatively charged PGS provided an electrostatically driven surface for anchoring the catalyst. First, as seen in Fig. 5b, the deposition of the nanosheets occurred randomly on the PGS surface. The interconnection between
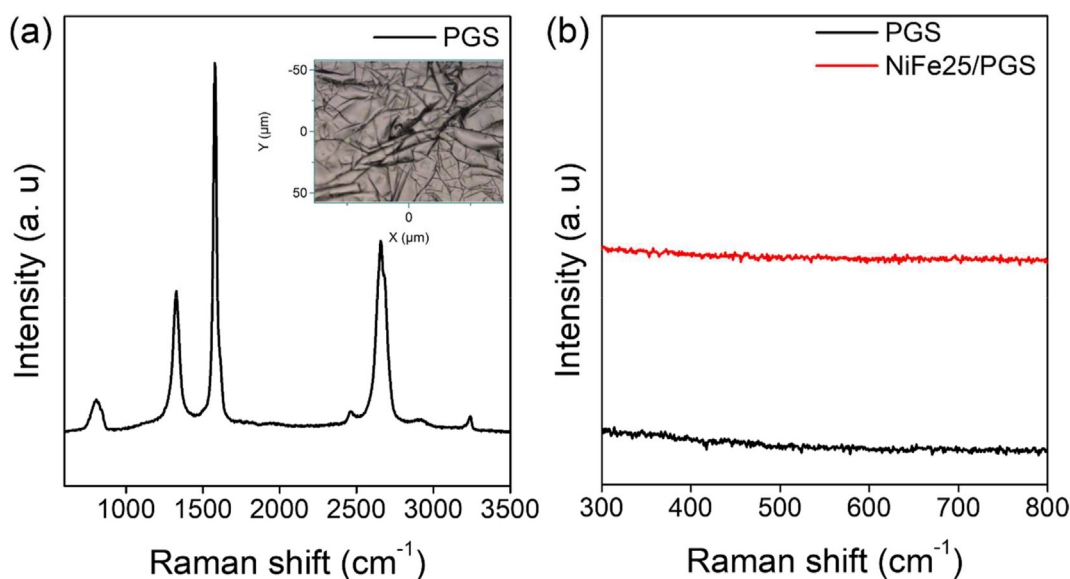

Fig. 2 − Raman spectra: (a) Commercial PGS; (b) NiFe25/PGS electrocatalyst.
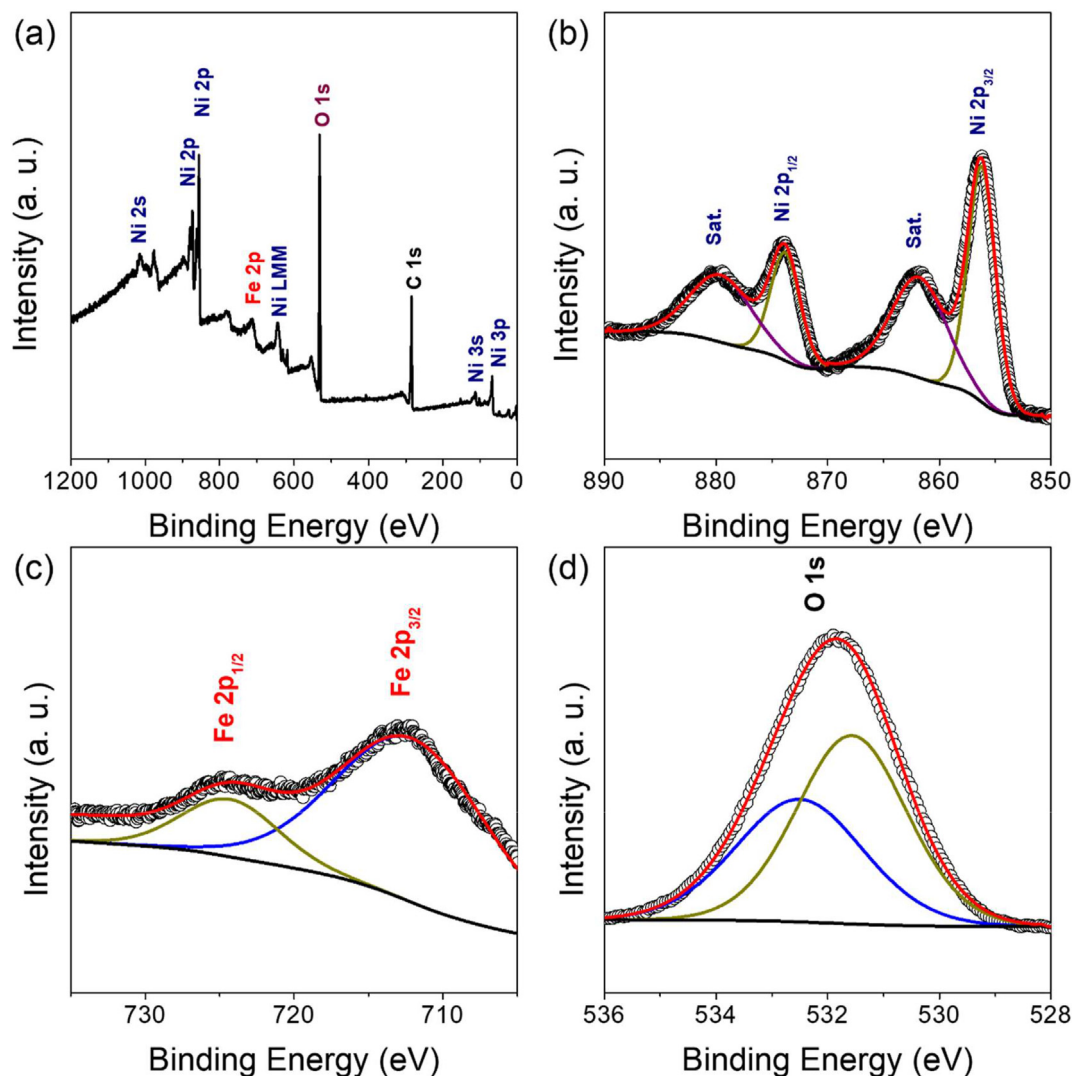
Fig. 3 — XPS spectra of NiFe25/PGS electrocatalyst: (a) Survey; (b) Ni 2p; (c) Fe 2p; (d) O 1s.
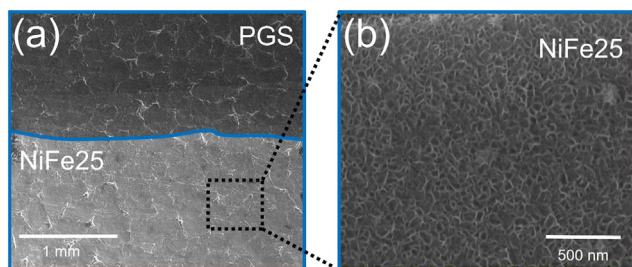

Fig. 4 — FESEM images of NiFe25/PGS electrocatalyst: (a) Backscattered electrons (BE) of NiFe25/PGS electrocatalyst; (b) Inset of the region of electrocatalyst using secondary electrons (SE) detector.

the nanosheets was observed with 25 s, followed by an increase in the catalytic film thickness.

For the complete study of the morphological and structural properties, the growth of the NiFe25 electrocatalyst on a carbon microscopy electron transmission (TEM) grid was proposed, and the analysis was performed using a STEM method.

Fig. 6a and b shows the images of high-angle annular dark-field imaging and bright-field imaging of NiFe25, respectively. The electrocatalyst grew on the carbon grid with nanosheet morphology, as observed in the results. The characteristic morphology corroborated with the previously published results [60]. Fig. 6c shows the energy-dispersive X-ray mapping. Notably, there was a good distribution of nickel and iron. The elementary analysis showed that the electrocatalyst contained ~75% and ~25% of nickel and iron, respectively, indicating that the electrodeposition was efficient in preparing the NiFe25 electrocatalyst, both on the PGS surface and TEM carbon grid.

A high-resolution STEM analysis was performed to evaluate the crystallinity of the material. Fig. 7a–c and Figures S7a, b show high-resolution images of NiFe25 deposited on the carbon grid. Growth of crystalline clusters in the nanosheets and some regions of the zone axis can be observed in Fig. 7a and Figures S7a. Fourier transform images (Fig. 7b) were acquired using the ImageJ software [61]. The interplanar distances of 0.15, 0.20, 0.21, 0.23, and 0.25 nm were assigned to the planes (110), (018), (107), (015), and (012), respectively. The
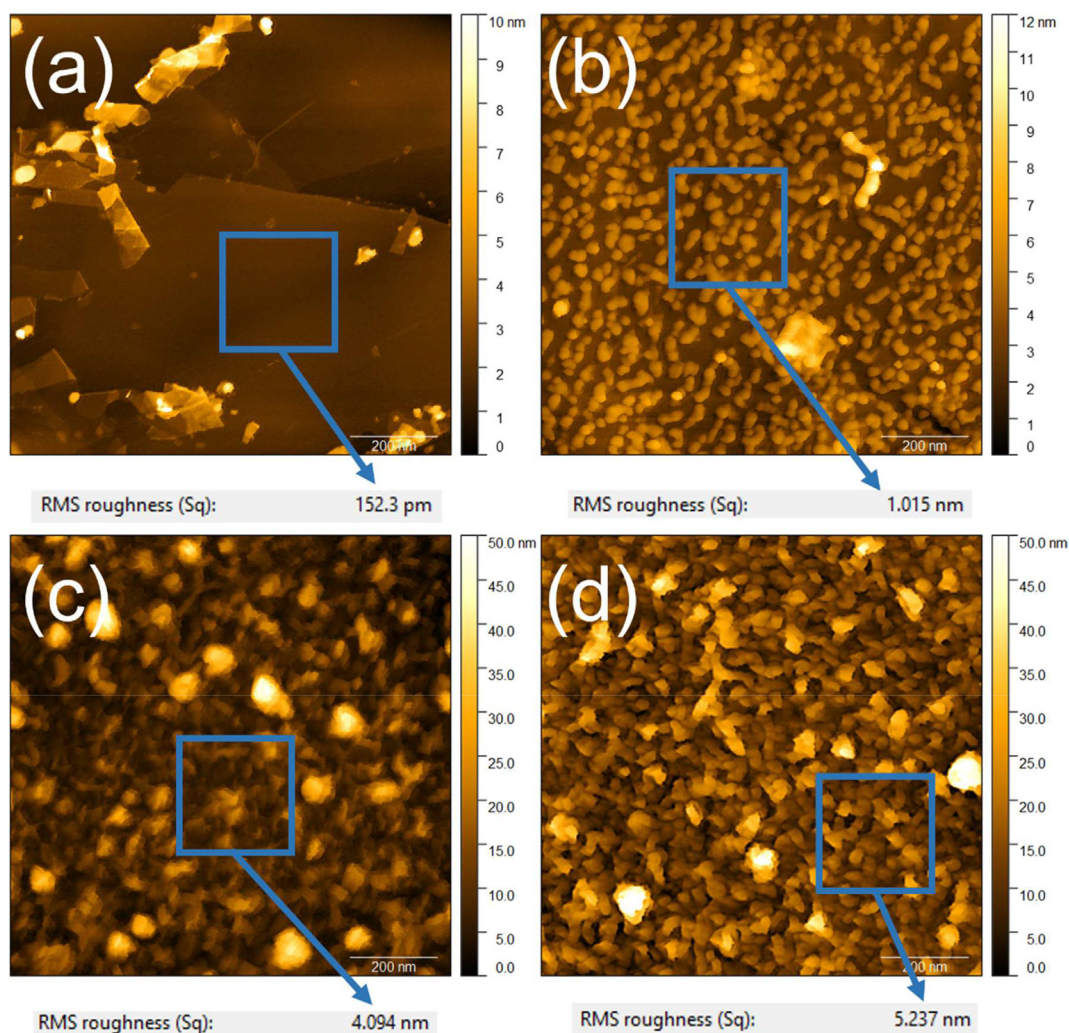
Fig. 5 — AFM images of NiFe25/PGS electrocatalyst in different deposition times: (a) PGS; (b) 10 s; (c) 25 s; (d) 50 s.

results agreed with the NiFe-LDH structure reported in previous studies [62–65]. The hypothesis about the growth of an ultrathin film of the catalyst is more plausible as the clusters showed high crystallinity, however, the diffraction patterns could not be observed in GIXRD.

To show the catalytic efficiency of NiFe25/PGS, a comparison was made with other catalysts, synthesized with 10% and 50% iron (NiFe10/PGS and NiFe50/PGS, respectively), and contained nickel or iron only (Ni/PGS and Fe/PGS, respectively). Before each electrochemical measurement, CV was performed at 10 mV s−1 to stabilize the surface of the catalysts. In Fig. S8a, the first five CV cycles for the NiFe25/PGS can be observed. There was no significant change in the redox process after the second stabilization cycle. The anodic peak (1.41 V *vs.* RHE) was assigned to the transformation of Ni(OH)2 into NiOOH, whereas the cathodic peak was attributed to the reverse transformation from NiOOH to Ni(OH)2 (1.34 V *vs.* RHE) [66].

Fig. S8b shows the CV curves obtained at different scanning rates (5–100 mV s−1) following stabilization. Notably, the increase in scan rate accompanied a displacement in the redox peaks and an increase in the current density. The anodic and cathodic peak currents have a linear relationship

with the square root of the scan rate (Fig. S8c). This suggests that redox reaction is a diffusion-controlled process, a characteristic of an ideal surface reaction [67]. Unlike CV curves showing an ideal rectangular shape found in double layer capacitors, this broad pair of redox current peaks is a pseudocapacitance feature from Faradaic redox reactions [68].

The deposition of the NiFe25 electrocatalyst on PGS was done for different durations to decide the optimal deposition time in terms of catalytic activity for OER. Fig. S9 shows the graph of η as a function of deposition time. The best catalytic activity was seen for 200 s of electrodeposition. Therefore, all materials for the OER study were prepared with this deposition time. Fig. 8a shows the CV curves for the hydroxyl oxidation reactions involving the electrocatalysts NiFe10/PGS, NiFe25/PGS, NiFe50/PGS, Ni/PGS, and Fe/PGS. All materials displayed efficient catalytic activities, indicating the possibility of using the electrocatalysts deposited electrochemically on PGS to catalyze oxygen evolution. Another relevant parameter is the influence of the structures on the mixture of the nickel and iron ions.

The sample containing only the Ni electrocatalyst showed an onset potential of 1.58 V *vs.* RHE, whereas for the sample with Fe, an onset potential of 1.63 V *vs.* RHE was observed. The
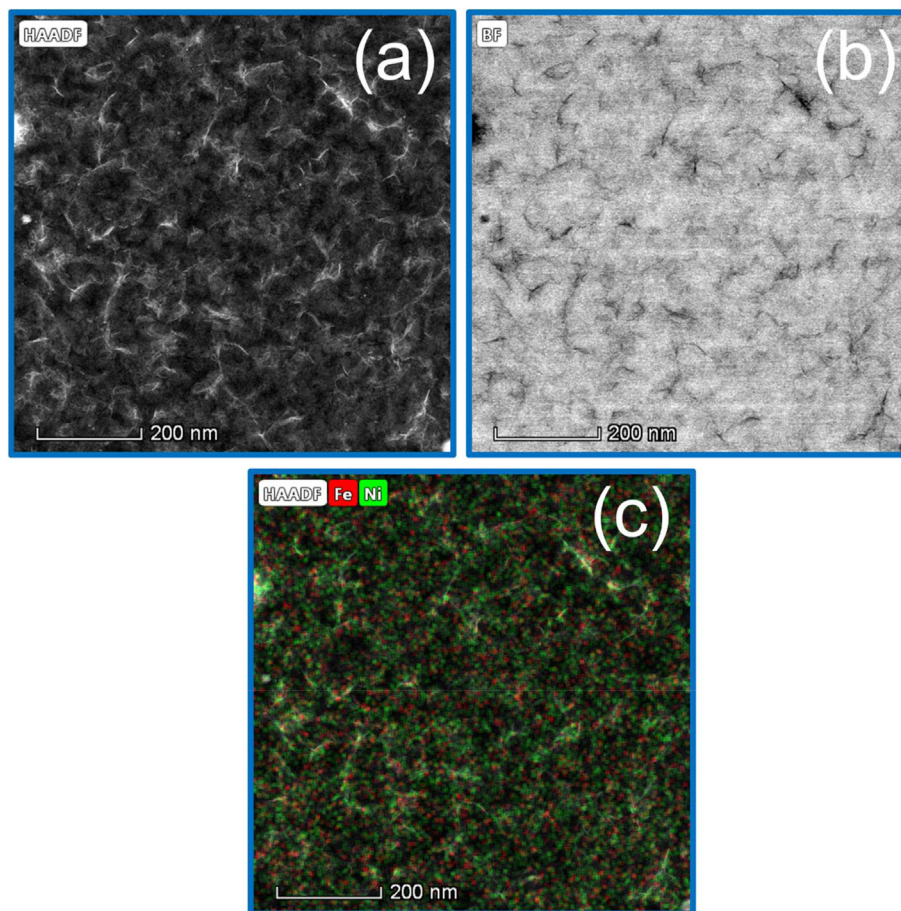
Fig. 6 − STEM images of NiFe25 electrocatalyst deposited on carbon grid: (a) High-angle annular dark-field imaging (HAADF); (b) bright-field (BF); (c) EDX mapping.

addition of Fe to the Ni-LDH structures shifted the onset potential close to 1.50 V *vs.* RHE. The maximum current densities found in the present study were in the decreasing order: NiFe25/PGS (119,12 mA cm−2)>NiFe50/PGS (111,63 mA cm−2) >NiFe10/PGS (100,92 mA cm−2)>Ni/PGS (41,64 mA cm^{-2})>Fe/ PGS (19,86 mA cm^{-2}). These values agreed with previous studies [69,70]. Emphasizing the peak region in the OER curves (Fig. 8b), the redox pair associated with Ni2+/Ni3+ was clearly seen for all samples except for Fe/PGS. This shows that Fe3+ ions remained unchanged during the hydroxyl oxidation process because no redox process occurred on the surface of the Fe/PGS catalyst.

A peak shift toward higher potentials and a decrease in the peak current density with increasing amounts of Fe within the structures was observed. The addition of Fe increased the potential necessary for the transformation of Ni(OH)2 to NiOOH. This displacement could also be attributed to the decreased affinity between the oxygen species and Ni sites on the surface caused by Fe3+ ions [71]. The decrease in the current density of the anodic and cathodic peaks was related to a decrease in the voltammetry charge, possibly due the substitution of Ni sites by Fe decreasing the specific oxidative charge [72].

To analyze the OER performances of the studied materials, the values of η were obtained at 10 mA cm−2 because the

performance of the electrocatalyst for oxygen production was evaluated with respect to the current density corresponding to 10% of the solar-to-fuel conversion [73]. Fig. 9a shows the average values of the overpotentials obtained from the OER curves for all samples. The average values of η are in the increasing order: NiFe25/PGS (332 mV)<NiFe50/PGS (350 mV) <NiFe10/PGS (352 mV)<Ni/PGS (439 mV)<Fe/PGS (526 mV). These results are in accordance with the literature and show that the electrocatalysts deposited on PGS are promising for hydroxyl oxidation in alkaline electrolytes because they are obtained in a facile and clean way. Table S2 shows the comparison of different results obtained for NiFe-LDH structures and other materials.

Fig. 9b shows the Tafel plots for all electrocatalysts deposited on PGS. The slopes were calculated from the linear portion of the OER curves using Equation 3:

$$\frac{\eta}{b} = log\frac{J}{J_0} \tag{3}$$

where b and $J0$ are the Tafel slope and the exchange current density, respectively.

The influence of Fe3+ ions on the Tafel slope values could be inferred from these results. The Ni/PGS catalyst had a Tafel slope of 55 mV dec^{-1}, whereas NiFe10/PGS, NiFe25/PGS, and NiFe50/PGS samples showed the values of 39, 33, and 34 mV
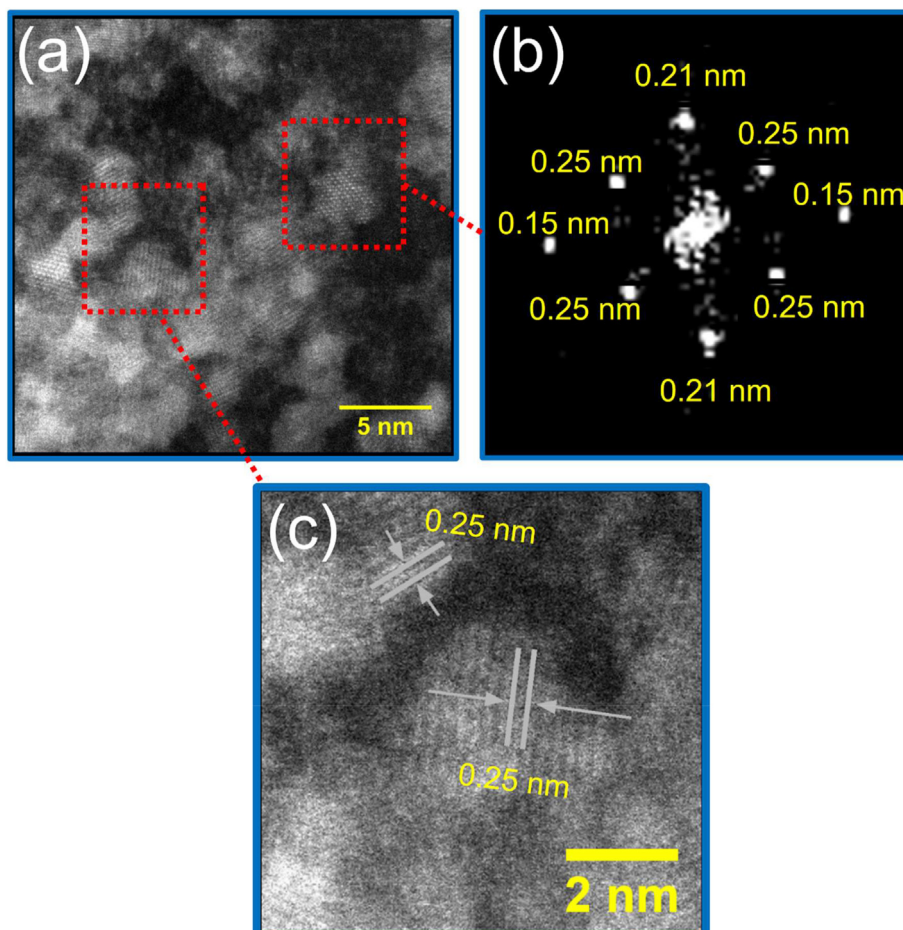
Fig. 7 – High resolution STEM images of NiFe25 electrocatalyst deposited on carbon grid.
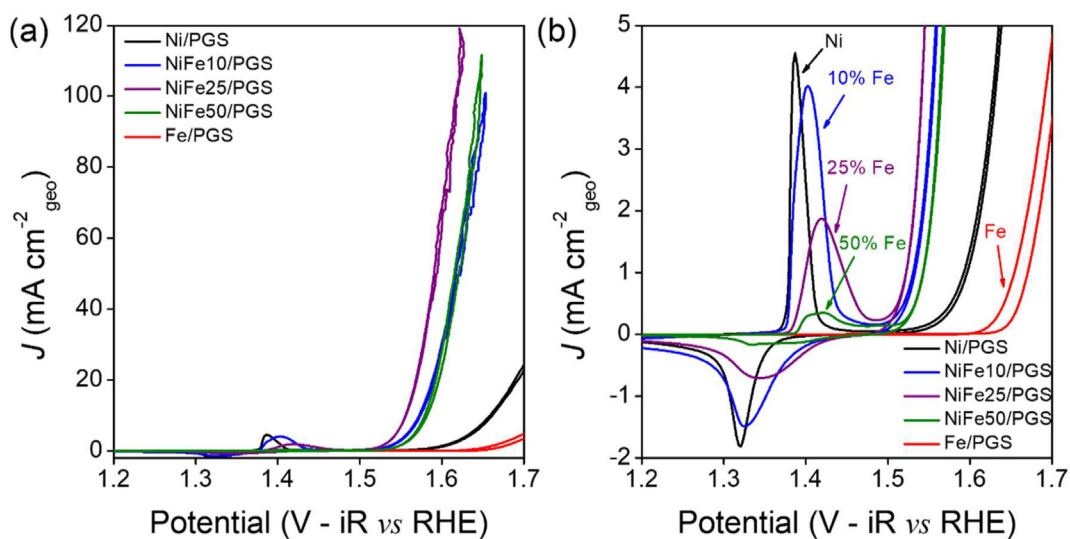

Fig. 8 – Electrochemical characterization of electrocatalysts deposited on PGS in NaOH 1 mol L^{-1}: (a) Current density (J) vs. potential (V −iR vs. RHE) curves; (b) Approximation in the Ni^{2+}/Ni^{3+} redox peak region.

dec^{-1}, respectively. The rate-determining step of a reaction with 30 mV dec^{-1} slope was associated with the transfer step of the third electron, whereas that with 60 mV dec−1 was

associated with a chemical reaction after the transfer of the first electron [9]. Alobaid et al. [74] reported that the most likely rate-determining step for NiFe-LDH in an alkaline
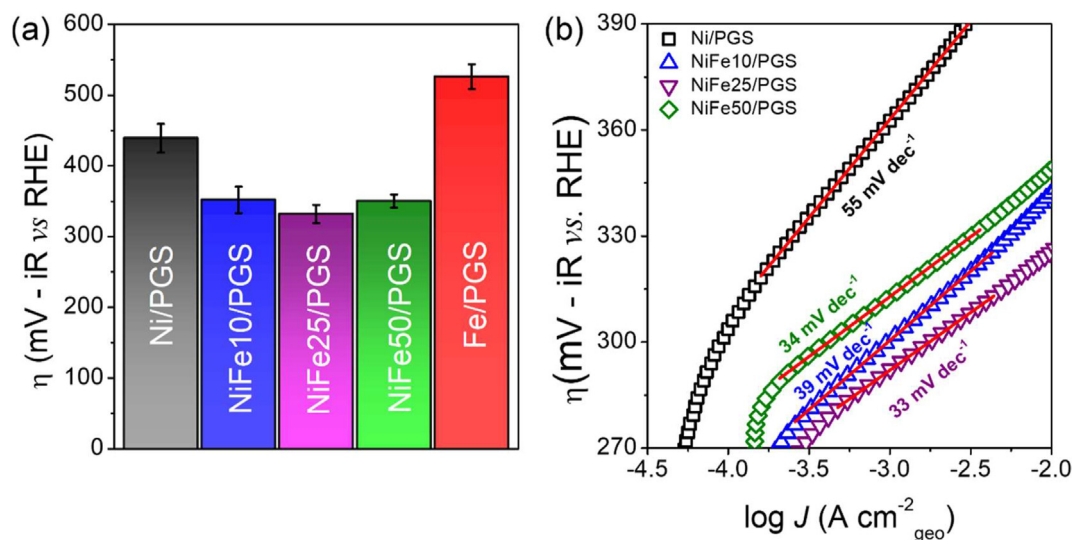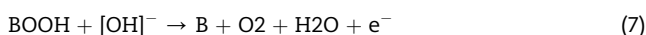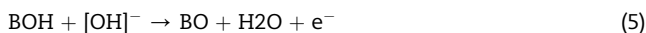
Fig. 9 – Electrochemical characterization of electrocatalysts deposited on PGS in NaOH 1 mol L^{-1}: (a) Overpotential (η) vs. amount of Fe; (b) Tafel plots (η vs. J).

electrolyte is the transfer of the third electron, which is related to the formation of the peroxide intermediate, BOOH, where B is the active site in Equation (6) below. Equations (4)–(7) show the mechanism of O2 production by the formation of peroxide intermediate:

$$B + [OH]^- \rightarrow BOH + e^- \quad (4)$$

$$BOH + [OH]^- \rightarrow BO + H2O + e^- \quad (5)$$

$$BO + [OH]^- \rightarrow BOOH + e^- \quad (6)$$

$$BOOH + [OH]^- \rightarrow B + O2 + H2O + e^- \quad (7)$$

According to the results presented in our study, Fe addition induces a change in the rate-determining step because the Ni/PGS electrocatalyst appears to have the second electron transfer step as determining, whereas the electrodes with Fe present the third electron transfer step as the most plausible. The electrocatalysts NiFe10/PGS, NiFe25/PGS, and NiFe50/PGS present themselves as very promising for OER.

For the complete study of electrochemical properties, an EIS analysis was performed. The Nyquist plots of electrocatalysts deposited on PGS are shown in Fig. 10a. Notably, the addition of Fe3+ ions influences the total resistance of the electrocatalyst. The electrodes of Ni/PGS and Fe/PGS do not show the complete semicircle because the applied potential is not sufficient for OER to occur efficiently. These materials have the slowest kinetics for oxygen evolution among the studied electrocatalysts. NiFe10/PGS, NiFe25/PGS, and NiFe50/PGS catalysts showed excellent results of catalytic efficiency for OER. However, the NiFe25/PGS sample showed the smallest semicircle, implying it is the sample with the lowest total resistance.

A potential of 1.6 V vs. RHE was applied to the NiFe25/PGS sample and a decrease in the semicircle was observed (Fig. S10), suggesting an increase in the catalysis of hydroxyl oxidation with increasing potentials [74]. Li et al. [75] reported that the decrease in the semicircle with increasing potentials corresponds to an increase in the overpotential for oxygen evolution processes occurring on the catalyst surface.

To calculate the values for charge transfer resistance (Rct), double layer capacitance (Cdl), adsorption resistance (Rads), and adsorption capacitance (Cads), an Armstrong and Henderson equivalent circuit fit was performed. To apply this model, resistive and capacitive elements were used. Figs. S11a–f shows the Nyquist plots of electrocatalysts NiFe10/PGS, NiFe25/PGS, and NiFe50/PGS fitted with the proposed equivalent circuit. The electrolyte resistance (Rel) was around 3 Ω for all catalysts. Results for NiFe10/PGS, NiFe25/PGS, and NiFe50/PGS electrodes can be seen in Table S3. The highest resistance values were found for NiFe50/PGS possibly due to the excess of Fe within the structure, inducing a decrease in the conductivity of the material. The NiFe25/PGS electrocatalyst had the lowest Rct and Rads values of 1.69 and 17.02 Ω, respectively. In addition, a decrease in the values of Cdl and Cads was observed with the increasing amounts of Fe. This can be associated with the decrease in the voltametric charge values, observed in the CV curves (Fig. 8b).

Although all samples showed good catalytic activities, NiFe25/PGS electrode showed the greatest potential because it presented a smaller value of η, a low Tafel slope, and the lowest Rct. Therefore, chronoamperometry was performed to evaluate the stability of the NiFe25/PGS catalyst (Fig. 10b). This result denotes good sample stability. At the beginning of chronoamperometry, this material had a current density of approximately 13 mA cm−2, which dropped to 9 mA cm−2 after 10 h of analysis. Fig. 10b inset shows bubbles at the electrocatalyst surface during the measurement of electrochemical stability.

To show the effectiveness of the PGS substrate in catalysis of OER, the NiFe25 sample was deposited on GC (NiFe25/GC) and fluorine-doped tin oxide (NiFe25/FTO) substrates using the same methods. The comparison among the different
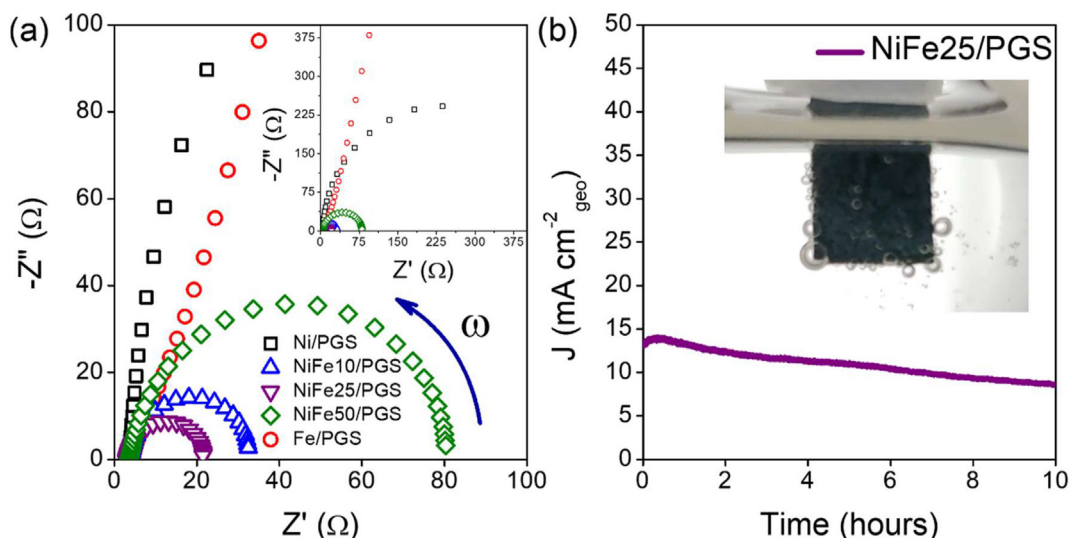
Fig. 10 – Electrochemical characterization of electrocatalysts deposited on PGS in NaOH 1 mol L⁻¹: (a) EIS measurements (Nyquist curves); (b) current density (J) vs. time (hours) curves for NiFe25/PGS electrocatalyst.

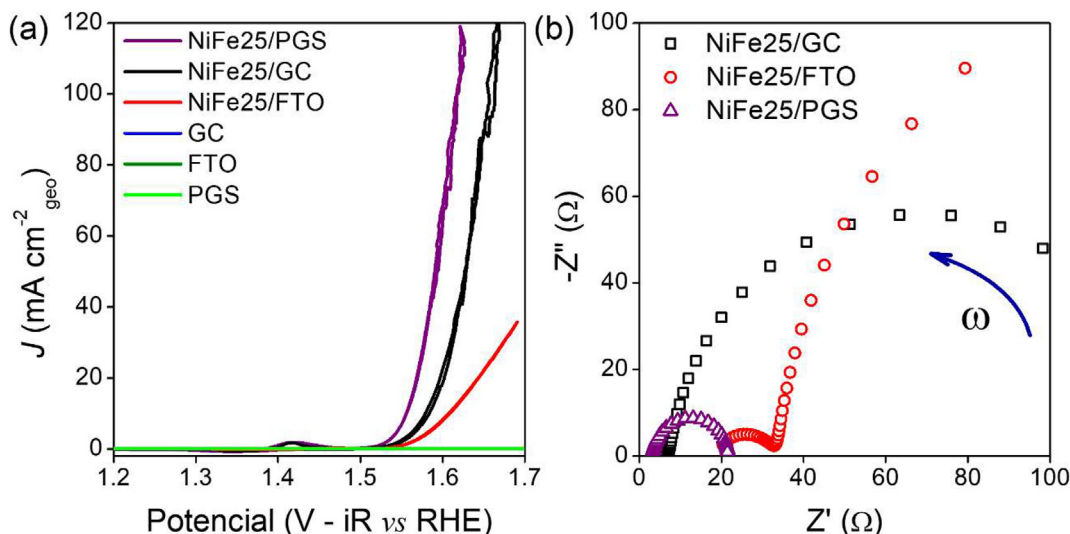**Fig. 11 – Electrochemical characterization of NiFe25 electrocatalyst deposited on PGS, GC and FTO in NaOH 1 mol L⁻¹: (a) Current density (J) vs. potential (V −iR vs. RHE) curves; (b) EIS measurements (Nyquist curves).**

substrates with the NiFe25 electrocatalyst can be seen in Fig. 11a and b. The influence of substrates on the catalytic performance is evident. NiFe25/PGS shows better OER performance compared to the same material deposited on GC and FTO (Fig. 11a). η values were calculated using Equation (2), and the results are presented in the decreasing order: NiFe25/PGS (320 mV) < NiFe25/GC (350 mV) < NiFe25/FTO (380 mV).

Fig. 11b shows the Nyquist plots of NiFe25 electrocatalysts deposited on PGS, GC, and FTO. A variation in R_{el} was observed depending on the substrate used. NiFe25/PGS showed 3.02 Ω, whereas NiF25/GC and NiFe25/FTO samples showed higher resistances of 6.98 and 18.31 Ω, respectively. R_{el} can be associated with internal resistances, such as electrolyte, separator, and current collector [75]. Because the separation between the working and reference electrodes was the same and the solution was not changed, changing the substrate, i.e., the

current collector affected the displacement of this resistance directly.

The total resistance of the sample deposited on PGS was much lower than the samples on GC and FTO. NiFe25/PGS catalyst had a total resistance approximately 16-fold and 7-fold less than NiFe/FTO and NiFe/GC, respectively. The fit for the NiFe25/GC and NiFe25/FTO samples was performed as well (Fig. S12d and Table S3). In agreement with the previous results, NiFe25/PGS (1.69 Ω) had a lower R_{ct} than NiFe25/GC (10.64 Ω) and NiFe25/FTO (15.65 Ω) electrodes.

Conclusion

The proposed methodology for the growth of the NiFe-LDH film on the PGS surface via electrodeposition proved to be

simple and efficient. The results supported the hypothesis of the growth of an ultrathin catalyst film on the surface of PGS. Crystalline NiFe-LDH nanoclusters were found in the structures grown on the carbon STEM grid, although it was not possible to observe the diffraction planes or vibration modes of the catalyst by GIXRD and Raman techniques. The electrochemical performances show that PGS acted as an excellent support electrode. NiFe25/PGS showed low overpotential (332 mV), low Tafel slope value (33 mV dec^{-1}), and the lowest Rct among the studied catalysts. An increase in Fe amounts in NiFe-LDH provided more interaction between Fe and Ni, contributing directly to the improvement of OER performance because this synergetic effect is essential to oxidize the hydroxyl efficiently. However, large amounts of Fe can increase the resistance, thus, decreasing effectiveness. Compared to other substrates, PGS is a better substrate/catalyst interface, improving the general OER catalysis. From an application point of view, PGS proves a potential support electrode candidate for hydroxyl oxidation reactions.

Declaration of competing interest

The authors declare that they have no known competing financial interests or personal relationships that could have appeared to influence the work reported in this paper.

Acknowledgments

Appendix A. Supplementary data

Supplementary data to this article can be found online at https://doi.org/10.1016/j.ijhydene.2021.12.245.

REFERENCES

[1] Badwal SPS, Giddey SS, Munnings C, Bhatt AI, Hollenkamp AF. Emerging electrochemical energy conversion and storage technologies. Front Chem 2014;2:1—28. https://doi.org/10.3389/fchem.2014.00079.

[2] Peng C, Ran N, Wan G, Zhao W, Kuang Z, Lu Z, et al. Engineering active Fe sites on nickel—iron layered double hydroxide through component segregation for oxygen evolution reaction. ChemSusChem 2020;13:811—8. https://doi.org/10.1002/cssc.201902841.

[3] Sapountzi FM, Gracia JM, Weststrate CJ, Kees J, Fredriksson HOA, Niemantsverdriet JW (Hans). Electrocatalysts for the generation of hydrogen, oxygen and synthesis gas. Prog Energy Combust Sci 2017;58:1—35. https://doi.org/10.1016/j.pecs.2016.09.001.

[4] Wojtyła S, Baran T. Electrochemically prepared copper/indium oxides photocathode for efficient photoelectrochemical hydrogen production. Sol Energy Mater Sol Cell 2020:206. https://doi.org/10.1016/j.solmat.2019.110262.

[5] Gao R, Yan D. Recent development of Ni/Fe-based micro/nanostructures toward photo/electrochemical water oxidation. Adv Energy Mater 2020;10:1—19. https://doi.org/10.1002/aenm.201900954.

[6] Nogueira AE, Santos Soares MR, Souza Junior JB, Ospina Ramirez CA, Souza FL, Leite ER. Discovering a selective semimetal element to increase hematite photoanode charge separation efficiency. J Mater Chem 2019;7:16992—8. https://doi.org/10.1039/c9ta05452a.

[7] Bhowmick S, Dhankhar A, Sahu TK, Jena R, Gogoi D, Peela NR, et al. Low overpotential and stable electrocatalytic oxygen evolution reaction utilizing doped perovskite oxide, La$_{0.7}$Sr$_{0.3}$MnO$_3$, modified by cobalt phosphate. ACS Appl Energy Mater 2020;3:1279—85. https://doi.org/10.1021/acsaem.9b02167.

[8] Kou T, Chen M, Wu F, Smart TJ, Wang S, Wu Y, et al. Carbon doping switching on the hydrogen adsorption activity of NiO for hydrogen evolution reaction. Nat Commun 2020;11:1—10. https://doi.org/10.1038/s41467-020-14462-2.

[9] Suen N-T, Hung S-F, Quan Q, Zhang N, Xu Y, Chen HM. Electrocatalysis for the oxygen evolution reaction: recent development and future perspectives. Chem Soc Rev 2017;46:337—65. https://doi.org/10.1039/C6CS00328A.

[10] Suntivich J, May KJ, Gasteiger HA, Goodenough JB, Shao-Horn Y. A perovskite oxide optimized for oxygen evolution catalysis from molecular orbital principles. Science 2011;334:1383—5. https://doi.org/10.1126/science.1212858.

[11] Zhu K, Zhu X, Yang W. Application of in situ techniques for the characterization of NiFe-based oxygen evolution reaction (OER) electrocatalysts. Angew Chem Int Ed 2019;58:1252—65. https://doi.org/10.1002/anie.201802923.

[12] Rebekah A, Ashok Kumar E, Viswanathan C, Ponpandian N. Effect of cation substitution in MnCo$_2$O$_4$ spinel anchored over rGO for enhancing the electrocatalytic activity towards oxygen evolution reaction (OER). Int J Hydrogen Energy 2020;45:6391—403. https://doi.org/10.1016/j.ijhydene.2019.12.164.

[13] Han X, Lin Z, He X, Cui L, Lu D. The construction of defective FeCo-LDHs by in-situ polyaniline curved strategy as a desirable bifunctional electrocatalyst for OER and HER. Int J Hydrogen Energy 2020;45:26989—99. https://doi.org/10.1016/j.ijhydene.2020.07.006.

[14] Zhang Y, Gao X, Lv L, Xu J, Lin H, Ding Y, et al. Tailoring π-symmetry electrons in cobalt—iron phosphide for highly efficient oxygen evolution. Electrochim Acta 2020;341:136029. https://doi.org/10.1016/j.electacta.2020.136029.

[15] Wang Y, Wu Q, Zhang B, Tian L, Li K, Zhang X. Recent advances in transition metal carbide electrocatalysts for oxygen evolution reaction. Catalysts 2020;10:1—30. https://doi.org/10.3390/catal10101164.

[16] Wang Y, Tao S, Lin H, Wang G, Zhao K, Cai R, et al. Atomically targeting NiFe LDH to create multivacancies for OER catalysis with a small organic anchor. Nano Energy 2020:105606. https://doi.org/10.1016/j.nanoen.2020.105606.

[17] Dionigi F, Zeng Z, Sinev I, Merzdorf T, Deshpande S, Lopez MB, et al. In-situ structure and catalytic mechanism of NiFe and CoFe layered double hydroxides during oxygen evolution. Nat Commun 2020;11:2522. https://doi.org/10.1038/s41467-020-16237-1.

[18] Lin Y, Wang H, Peng CK, Bu L, Chiang CL, Tian K, et al. Co-induced electronic optimization of hierarchical NiFe LDH for

oxygen evolution. Small 2020;16:1–9. https://doi.org/10.1002/smll.202002426.

[19] Subbaraman R, Tripkovic D, Chang KC, Strmcnik D, Paulikas AP, Hirunsit P, et al. Trends in activity for the water electrolyser reactions on 3d M(Ni,Co,Fe,Mn) hydr(oxy)oxide catalysts. Nat Mater 2012;11:550–7. https://doi.org/10.1038/nmat3313.

[20] Corrigan DA. The catalysis of the oxygen evolution reaction by iron impurities in thin film nickel oxide electrodes. J Electrochem Soc 1987;134:377–84. https://doi.org/10.1149/1.2100463.

[21] Trotochaud L, Young SL, Ranney JK, Boettcher SW. Nickel – iron oxyhydroxide oxygen-evolution electrocatalysts : the role of intentional and incidental iron. Incorporation 2014;136:6744–53. https://doi.org/10.1021/ja502379c.

[22] Görlin M, Chernev P, De Araújo JF, Reier T, Dresp S, Paul B, et al. Oxygen evolution reaction dynamics, faradaic charge efficiency, and the active metal redox states of Ni-Fe oxide water splitting electrocatalysts. J Am Chem Soc 2016;138:5603–14. https://doi.org/10.1021/jacs.6b00332.

[23] Louie MW, Bell AT. An investigation of thin-film Ni-Fe oxide catalysts for the electrochemical evolution of oxygen. J Am Chem Soc 2013;135:12329–37. https://doi.org/10.1021/ja405351s.

[24] Li Z, Wang X, Ren J, Wang H. NiFe LDH/Ti$_3$C$_2$T$_x$/nickel foam as a binder-free electrode with enhanced oxygen evolution reaction performance. Int J Hydrogen Energy 2021. https://doi.org/10.1016/j.ijhydene.2021.11.048.

[25] Sun C, Wang T, Sun C, Li F. Layered double (Ni, Fe) hydroxide grown on nickel foam and modified by nickel carbonyl powder and carbon black as an efficient electrode for water splitting. Int J Hydrogen Energy 2021. https://doi.org/10.1016/j.ijhydene.2021.11.160.

[26] Ma Y, Wang F-G, Fan R-Y, Wang H-Y, Yu W-L, Liu H-J, et al. Microwave rapid hydrolysis induced two-dimensional NiFeSe nanosheets for efficient oxygen evolution reaction. Int J Hydrogen Energy 2021;46:35311–8. https://doi.org/10.1016/j.ijhydene.2021.08.106.

[27] Chen Z, Liu X, Shen T, Wu C, Zu L, Zhang L. Porous NiFe alloys synthesized via freeze casting as bifunctional electrocatalysts for oxygen and hydrogen evolution reaction. Int J Hydrogen Energy 2021;46:37736–45. https://doi.org/10.1016/j.ijhydene.2021.09.059.

[28] Zou X, Wei X, Bao W, Zhang J, Jiang P, Ai T. Local electronic structure modulation of NiVP@NiFeV-LDH electrode for high-efficiency oxygen evolution reaction. Int J Hydrogen Energy 2021;46:32385–93. https://doi.org/10.1016/j.ijhydene.2021.07.111.

[29] Kim JE, Bae K, Park C, Jeong S, Kim J, Yoon J, et al. Nickel–iron hydroxide oxygen evolution electrocatalysts prepared by a simple chemical bath deposition method. Int J Hydrogen Energy 2021;46:20313–24. https://doi.org/10.1016/j.ijhydene.2021.03.172.

[30] Salmanion M, Najafpour MM. Dendrimer-Ni-Based material: toward an efficient Ni–Fe layered double hydroxide for oxygen-evolution reaction. Inorg Chem 2021;60:6073–85. https://doi.org/10.1021/acs.inorgchem.1c00561.

[31] Ding J, Han Y, Hong G. Tailoring the activity of NiFe layered double hydroxide with CeCO$_3$OH as highly efficient water oxidation electrocatalyst. Int J Hydrogen Energy 2021;46:2018–25. https://doi.org/10.1016/j.ijhydene.2020.10.075.

[32] Salmanion M, Najafpour MM. Structural changes of a NiFe-based metal-organic framework during the oxygen-evolution reaction under alkaline conditions. Int J Hydrogen Energy 2021;46:19245–53. https://doi.org/10.1016/j.ijhydene.2021.03.107.

[33] Sun P, Ma R, Bai X, Wang K, Zhu H, Sasaki T. Single-layer nanosheets with exceptionally high and anisotropic hydroxyl ion conductivity. Sci Adv 2017;3:e1602629. https://doi.org/10.1126/sciadv.1602629.

[34] Zhang W Da, Yu H, Li T, Hu QT, Gong Y, Zhang DY, et al. Hierarchical trimetallic layered double hydroxide nanosheets derived from 2D metal-organic frameworks for enhanced oxygen evolution reaction. Appl Catal B Environ 2020;264:118532. https://doi.org/10.1016/j.apcatb.2019.118532.

[35] Luo Y, Wu Y, Wu D, Huang C, Xiao D, Chen H, et al. NiFe-layered double hydroxide synchronously activated by heterojunctions and vacancies for the oxygen evolution reaction. ACS Appl Mater Interfaces 2020;12:42850–8. https://doi.org/10.1021/acsami.0c11847.

[36] Zhang W, Wu Y, Qi J, Chen M, Cao R. A thin NiFe hydroxide film formed by stepwise electrodeposition strategy with significantly improved catalytic water oxidation efficiency. Adv Energy Mater 2017;7. https://doi.org/10.1002/aenm.201602547.

[37] Li D, Hao G, Guo W, Liu G, Li J, Zhao Q. Highly efficient Ni nanotube arrays and Ni nanotube arrays coupled with NiFe layered-double-hydroxide electrocatalysts for overall water splitting. J Power Sources 2020;448:227434. https://doi.org/10.1016/j.jpowsour.2019.227434.

[38] Zhang Y, Yang M, Jiang X, Lu W, Xing Y. Self-supported hierarchical CoFe-LDH/NiCo$_2$O$_4$/NF core-shell nanowire arrays as an effective electrocatalyst for oxygen evolution reaction. J Alloys Compd 2020;818:153345. https://doi.org/10.1016/j.jallcom.2019.153345.

[39] Chakthranont P, Kibsgaard J, Gallo A, Park J, Mitani M, Sokaras D, et al. Effects of gold substrates on the intrinsic and extrinsic activity of high-loading nickel-based oxyhydroxide oxygen evolution catalysts. ACS Catal 2017;7:5399–409. https://doi.org/10.1021/acscatal.7b01070.

[40] Wei H, Liu J, Deng Y, Hu W, Zhong C. Studies on the effect of the substrate on the electrocatalytic performance of electrodeposited NiFe hydroxides for oxygen evolution reaction. Int J Electrochem Sci 2019;14:4173–84. https://doi.org/10.20964/2019.05.45.

[41] Ruan J, Zhao W, Wu L, Li X, Zheng X, Ye Q, et al. New insights into graphite paper as electrocatalytic substrate for oxygen evolution reaction. Appl Surf Sci 2017;396:1146–54. https://doi.org/10.1016/j.apsusc.2016.11.102.

[42] Lu S, Lian J, Zhang F, Jiang W, Hu Q, Li D, et al. Fe 40 Co 40 Se 20 glassy films supported on carbon fiber paper as electrocatalysts in the oxygen evolution reaction. J Electrochem Soc 2019;166:F620–6. https://doi.org/10.1149/2.1101910jes.

[43] Panasonic. "PGS" graphite sheets. n.d, https://na.industrial.panasonic.com/products/thermal-management/thermal-management/thermal-management-products/series/pgs-graphite-sheet-ssm/AYA0002?reset=1. [Accessed 16 January 2020].

[44] Nakamura S, Miyafuji D, Toda R, Matsui T, Fukuyama H. Characterization of pyrolytic graphite sheet: a new type of adsorption substrate for studies of superfluid thin films. J Low Temp Phys 2018;192:330–45. https://doi.org/10.1007/s10909-018-1983-3.

[45] Ng KL, Malik M, Azimi G. A New generation of rechargeable aluminum ion battery technology. ECS Trans 2018;85:199–206.

[46] Wen CY, Huang GW. Application of a thermally conductive pyrolytic graphite sheet to thermal management of a PEM fuel cell. J Power Sources 2008;178:132–40. https://doi.org/10.1016/j.jpowsour.2007.12.040.

[47] Gozzo CB, Soares MRS, Sczancoski JC, Nogueira IC, Leite ER. Investigation of the electrocatalytic performance for oxygen evolution reaction of Fe-doped lanthanum nickelate

deposited on pyrolytic graphite sheets. Int J Hydrogen Energy 2019;44:21659–72. https://doi.org/10.1016/j.ijhydene.2019.06.109.

[48] Trucano P, Chen R. Structure of graphite by neutron diffraction. Nature 1975;258:136–7. https://doi.org/10.1038/258136a0.

[49] Kole M, Dey TK. Investigation of thermal conductivity, viscosity, and electrical conductivity of graphene based nanofluids. J Appl Phys 2013;113. https://doi.org/10.1063/1.4793581.

[50] Rosenburg F, Ionescu E, Nicoloso N, Riedel R. High-Temperature Raman spectroscopy of nano-crystalline carbon in silicon oxycarbide. Materials 2018;11:93. https://doi.org/10.3390/ma11010093.

[51] Wu Z, Zou Z, Huang J, Gao F. NiFe2O4 nanoparticles/NiFe layered double-hydroxide nanosheet heterostructure array for efficient overall water splitting at large current densities. ACS Appl Mater Interfaces 2018;10:26283–92. https://doi.org/10.1021/acsami.8b07835.

[52] Dutta S, Indra A, Feng Y, Song T, Paik U. Self-supported nickel iron layered double hydroxide-nickel selenide electrocatalyst for superior water splitting activity. ACS Appl Mater Interfaces 2017;9:33766–74. https://doi.org/10.1021/acsami.7b07984.

[53] Li P, Duan X, Kuang Y, Li Y, Zhang G, Liu W, et al. Tuning electronic structure of NiFe layered double hydroxides with vanadium doping toward high efficient electrocatalytic water oxidation. Adv Energy Mater 2018;8. https://doi.org/10.1002/aenm.201703341.

[54] Lin B, Le H, Xu F, Mu S. NiFe LDH/CuO nanosheet: a sheet-on-sheet strategy to boost the active site density towards oxygen evolution reaction. RSC Adv 2020;10:27424–7. https://doi.org/10.1039/d0ra02985h.

[55] Qiu Z, Tai CW, Niklasson GA, Edvinsson T. Direct observation of active catalyst surface phases and the effect of dynamic self-optimization in NiFe-layered double hydroxides for alkaline water splitting. Energy Environ Sci 2019;12:572–81. https://doi.org/10.1039/c8ee03282c.

[56] Niedrig H. Physical background of electron backscattering. Scanning 1978;1:17–34. https://doi.org/10.1002/sca.4950010103.

[57] Lin Y, Wang H, Peng CK, Bu L, Chiang CL, Tian K, et al. Co-induced electronic optimization of hierarchical NiFe LDH for oxygen evolution. Small 2020;16:1–9. https://doi.org/10.1002/smll.202002426.

[58] Sun H, Zhang W, Li J, Li Z, Ao X, Xue K, et al. Rh-engineered ultrathin NiFe-LDH nanosheets enable highly-efficient overall water splitting and urea electrolysis. Appl Catal B Environ 2020:119740. https://doi.org/10.1016/j.apcatb.2020.119740.

[59] Cheng X-L, Jiang J-S, Jin C-Y, Lin C-C, Zeng Y, Zhang Q-H. Cauliflower-like α-Fe2O3 microstructures: toluene–water interface-assisted synthesis, characterization, and applications in wastewater treatment and visible-light photocatalysis. Chem Eng J 2014;236:139–48. https://doi.org/10.1016/j.cej.2013.09.089.

[60] Xue Y, Fishman ZS, Röhr JA, Pan Z, Wang Y, Zhang C, et al. Tunable nano-interfaces between MnOx and layered double hydroxides boost oxygen evolving electrocatalysis. J Mater Chem 2018;6:21918–26. https://doi.org/10.1039/c8ta07508e.

[61] ImageJ 1.52a. n.d, https://imagej.nih.gov/ij/. [Accessed 17 January 2020].

[62] Munonde TS, Zheng H, Nomngongo PN. Ultrasonic exfoliation of NiFe LDH/CB nanosheets for enhanced oxygen

evolution catalysis. Ultrason Sonochem 2019;59:104716. https://doi.org/10.1016/j.ultsonch.2019.104716.

[63] Gao Y, Zhao Z, Jia H, Yang X, Lei X, Kong X, et al. Partially reduced Ni^{2+}, Fe3+-layered double hydroxide for ethanol electrocatalysis. J Mater Sci 2019;54:14515–23. https://doi.org/10.1007/s10853-019-03964-0.

[64] Arif M, Yasin G, Shakeel M, Mushtaq MA, Ye W, Fang X, et al. Hierarchical CoFe-layered double hydroxide and g-C3N4 heterostructures with enhanced bifunctional photo/electrocatalytic activity towards overall water splitting. Mater Chem Front 2019;3:520–31. https://doi.org/10.1039/c8qm00677f.

[65] Jaśkaniec S, Hobbs C, Seral-Ascaso A, Coelho J, Browne MP, Tyndall D, et al. Low-temperature synthesis and investigation into the formation mechanism of high quality Ni-Fe layered double hydroxides hexagonal platelets. Sci Rep 2018;8:4–11. https://doi.org/10.1038/s41598-018-22630-0.

[66] Chen S, Duan J, Bian P, Tang Y, Zheng R, Qiao SZ. Three-Dimensional smart catalyst electrode for oxygen evolution reaction. Adv Energy Mater 2015;5:1–7. https://doi.org/10.1002/aenm.201500936.

[67] Xiao T, Wang S, Li J, Yang N, Li W, Xiang P, et al. Sulfidation of NiFe-layered double hydroxides as novel negative electrodes for supercapacitors with enhanced performance. J Alloys Compd 2018;768:635–43. https://doi.org/10.1016/j.jallcom.2018.07.279.

[68] Jiang L, Sui Y, Qi J, Chang Y, He Y, Meng Q, et al. Hierarchical Ni-Co layered double hydroxide nanosheets on functionalized 3D-RGO films for high energy density asymmetric supercapacitor. Appl Surf Sci 2017;426:148–59. https://doi.org/10.1016/j.apsusc.2017.07.175.

[69] Dong Y, Komarneni S, Zhang F, Wang N, Terrones M, Hu W, et al. "Structural instability" induced high-performance NiFe layered double hydroxides as oxygen evolution reaction catalysts for pH-near-neutral borate electrolyte: the role of intercalates. Appl Catal B Environ 2020;263:118343. https://doi.org/10.1016/j.apcatb.2019.118343.

[70] Dong YY, Ma DD, Wu XT, Zhu QL. Electron-withdrawing anion intercalation and surface sulfurization of NiFe-layered double hydroxide nanoflowers enabling superior oxygen evolution performance. Inorg Chem Front 2019;7:270–6. https://doi.org/10.1039/c9qi01367a.

[71] Dionigi F, Strasser P. NiFe-based (Oxy)hydroxide catalysts for oxygen evolution reaction in non-acidic electrolytes. Adv Energy Mater 2016;6. https://doi.org/10.1002/aenm.201600621.

[72] Forslund RP, Hardin WG, Rong X, Abakumov AM, Filimonov D, Alexander CT, et al. Exceptional electrocatalytic oxygen evolution via tunable charge transfer interactions in La$_{0.5}$Sr$_{1.5}$Ni$_{1-x}$Fe$_x$O4 Ruddlesden-Popper oxides. Nat Commun 2018;9:3150. https://doi.org/10.1038/s41467-018-05600-y.

[73] McCrory CCL, Jung S, Peters JC, Jaramillo TF. Benchmarking heterogeneous electrocatalysts for the oxygen evolution reaction. J Am Chem Soc 2013;135:16977–87. https://doi.org/10.1021/ja407115p.

[74] Alobaid A, Wang C, Adomaitis RA. Mechanism and kinetics of HER and OER on NiFe LDH films in an alkaline electrolyte. J Electrochem Soc 2018;165:J3395–404. https://doi.org/10.1149/2.0481815jes.

[75] Li G, Anderson L, Chen Y, Pan M, Abel Chuang PY. New insights into evaluating catalyst activity and stability for oxygen evolution reactions in alkaline media. Sustain Energy Fuels 2018;2:237–51. https://doi.org/10.1039/c7se00337d.